Physics Letters A 387 (2021) 127007

Contents lists available at ScienceDirect

Physics Letters A

www.elsevier.com/locate/pla

Theoretical approach to quantum cascade micro-laser broadband multimode emission in strong magnetic fields

Aleksandra Gajić [a,*], Jelena Radovanović [b], Nikola Vuković [b], Vitomir Milanović [b], Dmitri L. Boiko [c]

[a] Vip mobile d.o.o., Belgrade, Serbia
[b] School of Electrical Engineering, University of Belgrade, Serbia
[c] Centre Suisse d'Electronique et de Microtechnique (CSEM), Neuchâtel, Switzerland

ARTICLE INFO

Article history:
Received 16 June 2020
Received in revised form 22 October 2020
Accepted 3 November 2020
Available online 10 November 2020
Communicated by S. Khonina

Keywords:
Quantum cascade laser (QCL)
Risken-Nummendal-Graham-Haken (RNGH) instability threshold
Self-pulsation
Quantum engineering
Micro-lasers

ABSTRACT

We have theoretically explored the influence of the magnetic field on supporting the multimode Risken-Nummendal-Graham-Haken (RNGH) self-pulsations seen in the optical spectrum as two broad modulations sidebands at the Rabi flopping frequency [25–27]. On the example of microcavity quantum cascade lasers (μ-QCLs), we demonstrate that Landau quantization in an external magnetic field slows down the effective decoherence and diffusion rates. The pump current required to reach the broadband multimode RNGH self-pulsations is lowered with the magnetic field strength, while the Rabi flopping frequency and the overall optical spectrum width remain practically unchanged. Our theoretical results indicate that an external magnetic field can be a valuable tool for achieving high-power broadband QCL self-pulsations in practice.

1. Introduction

Quantum Cascade Lasers (QCLs) provide one of the finest examples of how quantum engineering of interchangeable semiconductor layers can be employed in order to create powerful and adaptable light emitting sources in a broad spectrum of wavelengths tailored to a specific predefined use. Since their inception by Bell Laboratories [11], they have managed to prove the versatility of possible applications ranging from chemical sensing, medical diagnostics and optical communications, to high-sensitive real-time measurements of air polluting, greenhouse and poisonous gases. The realization of a device whose output characteristics are tuned by varying the layer composition and the thickness of constituent semiconductor materials sets a brilliant example of bandgap engineering and is made possible by the development of sophisticated material growth techniques [9,21].

The charge carrier dynamic in these complex device structures is very different from that occurring in inter-band lasers, and is governed by different mechanisms. In the active region of QCLs, where radiative transitions take place, the electron-longitudinal optical (LO) phonon scattering prevails. Such radiative transitions are characterized by extremely short carrier lifetimes, in the order of one picosecond [5], which in return result in high lasing threshold currents. This disadvantage can be overcome in device structures with further reduced charge carrier system dimensionality, for instance by applying a strong magnetic field in the growth direction of the epitaxial layers [5,8], [25–27], [5,1]). Under the influence of the magnetic field, the two-dimensional electron energy subbands are split into a series of discrete Landau levels (LLs) and an additional quantization of the electron in-plane motion is introduced. Taking into account that the scattering processes between two electron states depend on their energy difference, simple variation of the magnetic field strength can lead to suppression or enhancement of specific relaxation processes, enabling the device output characteristics to be tailored for a specific application needs. This feature, for instance, can be of particular importance for spectroscopic applications of QCL frequency combs in multimode operation regime [16].

* Corresponding author at: Cara Lazara 28, Pančevo 26000, Serbia.
E-mail address: a.gajic@vipmobile.rs (A. Gajić).

https://doi.org/10.1016/j.physleta.2020.127007
0375-9601/

In recent years, considerable effort has been put into research and fabrication of reliable room temperature operating compact QCL devices capable to produce short terahertz pulses [20,24]. This has been achieved using different approaches to generate frequency combs consisting of well-controlled equidistant frequency lines [19,7]. However, due to extremely short non-radiative lifetimes, pulse mode-locking operation is more difficult to occur in mid-infrared QCLs than in terahertz devices [34,4]. One of the possible ideas to overcome this problem has emerged with the proposal of QCL dynamics tailoring in such a way so as to produce regular Risken-Nummendal-Graham-Haken (RNGH) self-pulsations [30,2].

Low-threshold RNGH instability has been experimentally observed in both ridge waveguide QCLs as well as in buried heterostructure QCLs [33,13,6] and these experimental observations were in disagreement with the originally proposed theory of high-threshold RNGH instability in a laser [22,15]. In our recent studies [32,30] the multimode RNGH instability in a Fabry-Pérot cavity QCL has been analyzed in detail and a mechanism responsible for low-threshold RNGH instability in QCLs was proposed. It was shown that multimode RNGH instability occurs at the Rabi flopping frequency as a result of a combined effect of the carrier coherence grating, carrier population grating and relaxation processes due to carrier diffusion. In combination with the possibility of tailoring these features by the applied magnetic field, which we analyze in the present paper, these findings may lay down a foundation for a novel valuable tool in the design of QCLs tailored for specific applications.

2. Theoretical considerations

2.1. Relaxation and diffusion in magnetic field

In a QCL structure exposed to a strong magnetic field B applied along the growth direction, the continuous energy subbands $E_n(k_\parallel)$ are split into a series of discrete Landau levels with the energies defined as $E_{n,l} = E_n(k_\parallel = 0) + (l + 1/2)(\hbar eB)/(m_{\parallel,n}(E_{n_0})) - 1/8[(8l^2 + 8l + 5)\langle\alpha_0\rangle + (l^2 + l + 1)\langle\beta_0\rangle](\hbar eB/m^*)^2$, where index $l = 0, 1, 2, \dots$ enumerates Landau levels, $\omega_c = eB/m_{\parallel,n}(E_{n_0})$ is the cyclotron frequency, in which $m_{\parallel,n}(E_{n_0})$ denotes the parallel effective mass at the bottom of the n-th subband, m^* represents the parabolic effective mass in the quantum well material, and $\langle\alpha_0\rangle$, $\langle\beta_0\rangle$ are the nonparabolicity parameters averaged over the z-axis direction (epitaxial growth direction) [25–27]. As a model system, we consider a structure design with a 4QW active region in which double-LO phonon represents the dominant depopulation mechanism of the lower lasing level. The energy spacing between the three lowest-energy states in the active region matches the LO-phonon energy, facilitating the relaxation processes.

The LO-phonon emission rate on the transition between the initial $E_i = E_{n_i,l_i}$ and the final state $E_f = E_{n_f,l_f}$ is given by the following expression [5]:

$$W^{\mathrm{LO}}_{E_i \longrightarrow E_f} = \frac{e^2\omega_{\mathrm{LO}}}{4\varepsilon_0\varepsilon_p}\frac{1}{\delta\sqrt{2\pi}}\exp\left(-\frac{(E_i - E_f - \hbar\omega_{\mathrm{LO}})^2}{2\delta^2}\right)(N_q + 1)\int_0^\infty |F(q_\parallel)|^2 G(q_\parallel)dq_\parallel \tag{1}$$

where $\varepsilon_{\mathrm{p}}^{-1}$ denotes the difference between the reciprocal values of the static and the high-frequency dielectric constants ($\varepsilon_\infty = 10.67$ and $\varepsilon_s = 12.51$), $\hbar\omega_{\mathrm{LO}}$ is the LO-phonon energy, while δ stands for the width of the Gaussian distribution of the energy difference $E_i - E_f$. $N_q = 1/[\exp(\hbar\omega_{\mathrm{LO}}/k_BT) - 1]$ represents the mean number of LO phonons and $q_\parallel$ corresponds to the in-plane component of the phonon wave vector $\vec{q} = (q_\parallel, q_z)$. The quantity $|F(q_\parallel, l_i, l_f)|$ embodies the lateral overlap integral, which, in the case of $l_i \le l_f$, reads:

$$\left|F(q_\parallel, l_i, l_f)\right|^2 = \exp\left(-\frac{q_\parallel^2}{2\beta^2}\right)\frac{l_i!}{l_f!}\left(\frac{q_\parallel^2}{2\beta^2}\right)^{l_i - l_f}\left[L_{l_i}^{l_i - l_f}\left(\frac{q_\parallel^2}{2\beta^2}\right)\right]^2 \tag{2}$$

where $\beta = (eB/\hbar)^{-1/2}$ is the magnetic-field length, and $L_n^k(x)$ denotes the associated Laguerre polynomial. $G(q_\parallel) = \iint \eta_i^*(z)\eta_f(z) \times \eta_i(z')\eta_f^*(z')e^{-q_\parallel|z-z'|}dzdz'$ represents the form factor, and η_i and η_f stand for the z-dependent parts of the initial and final state wavefunctions, respectively.

Due to the monolayer thickness fluctuations, the interface roughness scattering (IRS) occurs at the interfaces of epitaxial layers. IRS rate can be estimated using the following expression [18,29,10]:

$$W^{IRS}_{E_i \longrightarrow E_f} = \frac{\sqrt{2\pi}}{\hbar\delta}\exp\left[(E_i - E_f)^2/2\delta^2\right]\sum_{k_{x_i},k_{x_f}}\left\langle|M_{i,f}|^2\right\rangle \tag{3}$$

Here, $\langle|M_{i,f}|^2\rangle = \frac{|F_{i,f}|^2\Lambda\Delta^2\sqrt{\pi\alpha}}{L_x}\exp(-\frac{\Delta k_x^2}{2}[\frac{2+\Lambda^2\beta^2}{2\beta^2}]) \cdot \varsigma(\Delta k_x)$ stands for the averaged squared scattering matrix element for the perturbation Hamiltonian in the form $\hat{H}_{IRS} = U_0 \cdot \delta(z - z_i) \cdot \Delta(x, y)$. In the expression describing the matrix element, $\Delta^2(\mathbf{r})$ represents the interface roughness height squared (at some in-plane position $\mathbf{r} = (x, y)$), Λ stands for the correlation length and L_x is the length of the structure in the x-axis direction. $\Delta k_x = k_{x_i} - k_{x_f}$ and $F_{i,f} = U_0\eta_i^*(z)\eta_f(z)$, while $\alpha = \beta^2/(\pi l_f!l_i!2^{l_i+l_f})$. The form factor ς is given by [10]:

$$\begin{aligned}\varsigma(\Delta k_x) = \iint \exp\left(-\beta^2\left[t^2 + (t-u)^2\right] - \frac{u^2}{\Lambda^2}\right) \cdot H_{l_i}\left[\beta t - \frac{\Delta k_x}{2\beta}\right] \cdot H_{l_i}\left[\beta(t-u) - \frac{\Delta k_x}{2\beta}\right] \cdot H_{l_i}\left[\beta t + \frac{\Delta k_x}{2\beta}\right] \\ \cdot H_{l_i}\left[\beta(t-u) + \frac{\Delta k_x}{2\beta}\right]dudt\end{aligned} \tag{4}$$

In the above expression, H_j is the Hermite polynomial of the order j. The averaged matrix element is a function of the wave vector component difference of the initial and final states. Therefore after averaging over k_{x_i} the following expression can be obtained:

$$\sum_{k_{x_i},k_{x_f}} \left\langle |M_{i,f}|^2 \right\rangle \longrightarrow \frac{L_x}{2\pi} \int_{-\infty}^{\infty} |M_{i,f}|^2 d(\Delta k_x) \tag{5}$$

The overall scattering rates in our model system are then approximated by taking into account just these two dominant scattering mechanisms, the LO-phonon scattering [14] and the IRS, as $W_{E_i \to E_f} = W^{\mathrm{LO}}_{E_i \longrightarrow E_f} + \sum_{z_i} \langle W^{IRS}_{E_i \longrightarrow E_f} \rangle$. In complex quantum cascade laser structures, many other different scattering mechanisms are present, such as electron-electron (ee), longitudinal acoustic phonon, alloy disorder, and ionized impurities scattering [29]. For instance, ee scattering becomes important at high carrier concentrations, when it has to be taken into account alongside with LO phonon scattering [17]. However, in our first study on the magnetic field effect on the RNGH instability in QCL, we consider a simpler case of low and moderate carrier concentrations [12], when ee scattering is not a dominant mechanism contrary to the LO and IRS processes. All other scattering processes are assumed to be of lesser importance in our model system, which allows us to easily calculate the longitudinal relaxation time T_1 and the diffusion coefficient D, as $D/\mu = kT/e$, where $\mu = eT_1/m$, represents the dipole matrix element of the lasing transition

The transverse relaxation time T_2 is obtained following the steps from Refs. [3,35] and using the following expression for the dephasing scattering rate:

$$W_\varphi = \frac{\pi}{4} \frac{k_B^2 T^2}{B_{coef} \hbar E_F} \left\{ \ln\left(\frac{2E_F}{k_B T}\right) + \frac{3(F_0^\sigma)}{(1+F_0^\sigma)^2} \ln\left(\frac{E_F}{k_B T \sqrt{b(F_0^\sigma)}}\right) \right\} \tag{6}$$

Here, $b(F_0^\sigma) = (1 + (F_0^\sigma)^2)/(1 + F_0^\sigma)^2$, B_{coef} represents a numerical coefficient which varies from 0.84 for weak magnetic fields to 0.79 for strong fields (see [3] for the characteristic values of the weak and strong fields) and the constant of electron-electron interaction F_0^σ is calculated according to the expression from Ref. [35]:

$$F_0^\sigma = -\frac{1}{\pi} \frac{r_s}{\sqrt{r_s^2 - 2}} \arctan \sqrt{\frac{1}{2} r_s^2 - 1} \tag{7}$$

for in this case $r_s^2 > 2$, since the gas parameter of the system equals $r_s = \sqrt{2} e^2 / \varepsilon \hbar V_F$ and V_F is evaluated as $V_F = \sqrt{2E_F/m_w}$, where E_F represents the Fermi level energy, and m_w is the effective mass in the quantum well material. The value of the Fermi level energy is obtained by numerically solving the equation describing the total sheet carrier density:

$$N_S = \frac{eB}{2\pi\hbar} \sum_{n,l} f_{FD}(E_{n,l}, E_F) \tag{8}$$

where $f_{FD}(E_{n,l}, E_F) = 1/(e^{(E_{n,l} - E_F)/(k_B T)} + 1)$. Calculating the transverse relaxation time in a non-equilibrium case would be extremely theoretically and computationally demanding, so an approximation of stability has been made in the case of equations (6) and (8), and an equilibrium Fermi level has been used.

It has been shown that under typical conditions, the effect of electron temperature on the gain is similar to that of the lattice temperature [12]. Like in [12], for the purpose of our exploratory study on the magnetic field effect on the RNGH instability in QCL we have assumed that the electron temperature and the lattice temperature coincide, i.e. $T_e = T_L$. This is a rather good simplifying assumption for the room-temperature operating conditions and up to moderate carrier concentrations [14]. In highly non-equilibrium conditions at a high carrier concentration, the electron temperature exceeds the lattice temperature and defines the optical gain [17]. The hot carrier effect in the presence of magnetic field is a standalone topic that deserves more detailed research and is left for another study.

2.2. Multimode RNGH instability

The occurrence of the multimode RNGH self-pulsations in a continuous-wave (CW) single-mode laser is attributed to parametric gain sidebands at Rabi flopping frequencies induced by coupled oscillations of the optical field, carrier coherences and populations [23]. The gain curve is restructured and widened, providing enough optical gain for other longitudinal modes to lase. The lasing behavior below and the laser dynamics above the RNGH instability threshold differ significantly from each other. Below the RNGH threshold, the optical mode is under the control of the optical cavity. However, above the RNGH instability threshold, the buildup of Rabi oscillations points toward the conclusion that now the optical field in the laser cavity is under the influence of a macroscopic polarization in the optical gain medium [15].

The analytical expression for the RNGH instability threshold is explained in [30]. Below we provide a brief summary relevant for the work presented here.

With the purpose of obtaining the gain curve for instabilities in initially non-lasing cavity modes, a linear stability analysis with respect to small perturbations in the main lasing mode is applied to the Maxwell-Bloch equations [22,15]. The standing wave pattern of the optical field in the cavity is taken into account. The perturbations are then recast in the form of propagating wavelets $\propto \exp(-i n_g \Omega z/c + \Lambda t)$, where Λ represents the Lyapunov exponent, $\Omega n_g/c$ is the detuning of the propagation constant from the main lasing mode and n_g is the group velocity index, while the parameter Ω represents the frequency offset [32]. The resulting linearized system of differential equations is then defined by a 9×9 block-block-diagonal matrix $M_{9\times 9}$ [32], whose largest eigen value provide the dispersion curve of the instability increment $\mathrm{Re}(\Lambda)$ as a function of the offset frequency Ω:

$$\mathrm{Re}(\Lambda_{\max}) = -\frac{1}{2\tau} + \frac{C_0(p)}{\Omega^2 + 1/T_{2,eff}^2} + \frac{C_1(p)}{\Omega^2 + A(p)^2} + \frac{C_2(p)}{\Omega^2 + 1/T_{2,eff}^2} + \frac{C_3(p)}{(\Omega^2 + 1/T_{2,eff}^2)^2} \tag{9}$$

Here, the coefficients $C_i(p)$ and $A(p)$ are independent of the offset frequency [they can be found in Appendix B of Ref. [31]], $T_{2,eff}$ is the effective transverse relaxation time, given by $T_{2,eff} = 1/(T_2^{-1} + Dk^2)$, and $\tau = n_g/cl_0$ is the photon lifetime in the cavity, where l_0

represents the cavity loss coefficient and n_g the group refractive index The dispersion curve has a symmetric shape with two maxima at the offset frequencies $\pm\Omega_{max}$ with Ω_{max} being very close to the Rabi flopping frequencies

$$\Omega_{\max} \approx \Omega^2_{Rabi}\sqrt{\frac{1}{2}\frac{T_{2,g}}{T_{2,eff}}\left(1+\frac{2}{\Omega^2_{Rabi}T_gT_{2,g}}\right)-\frac{1}{T_g^2}} \tag{10}$$

while the maximum increment value for the multimode RNGH instability can be estimated using an approximate expression:

$$\mathrm{Re}(\Lambda_{\max})|_{\Omega=\Omega_{\max}} = -\frac{1}{2\tau}\left(1-\frac{3}{2}\frac{\Omega^2_{Rabi}T^2_{2,eff}}{2}\right)+\frac{2\nu_0-1}{2\tau}\left[1-\Omega^2_{\max}T^2_{2,eff}-\frac{T^2_{2,eff}}{T_g^2}\right]^2 \tag{11}$$

Here, the effective relaxation times are given with $T_g=(T_1^{-1}+4Dk^2)^{-1}$ and $T_{2,g}=(T_2^{-1}+9Dk^2)^{-1}$ [32]. As can be appreciated from the instability gain curve, within an accuracy to the roundtrip phase self-repetition condition, the RF power spectrum of steady–state RNGH self-pulsations is centered near the Rabi flopping frequency. Because of the broadband gain spectrum (9), the phase self-repetition condition and the cavity mode selection is not crucial in long-cavity QCLs (mm-length) revealing multimode RNGH instability. However, these constraints become very important in micro-cavity QCLs (hundreds of micron long), capable to produce regular RNGH self-pulsations at Ω_{Rabi} (or its harmonics):

$$\Omega_{Rabi}=\sqrt{2}E=\sqrt{\frac{p-\upsilon_0}{T_1T_{2,eff}}} \tag{12}$$

where E stands for the normalized field amplitude of the optical wave in the cavity, $E=\sqrt{(p-\upsilon_0(p))/(2T_1T_{2,eff})}$ and the coefficient $\sqrt{2}$ appears due to the standing wave pattern of the optical field in the cavity, while p represents the pump rate normalized to the lasing threshold in the absence of spatial hole burning (SHB) i.e. $p=I/I_{th}$. The parameter υ_0 accounts for the SHB effect [32], which lowers the optical gain, increases the effective lasing threshold and reduces the slope efficiency of QCL:

$$\nu_0=\frac{1}{2}\left(p+1+\frac{T_{2,eff}}{T_{2,g}}+\frac{2T_1T_{2,eff}}{T_gT_{2,g}}\right)-\sqrt{\frac{1}{4}\left(p+1+\frac{T_{2,eff}}{T_{2,g}}+\frac{2T_1T_{2,eff}}{T_gT_{2,g}}\right)^2-p\cdot\left(1+\frac{T_{2,eff}}{T_{2,g}}\right)-\frac{2T_1T_{2,eff}}{T_gT_{2,g}}} \tag{13}$$

By combining Eq. (12) and (13) we find:

$$p-\nu_0=\frac{T_1T_{2,eff}}{T_gT_{2,g}}\left[\sqrt{1+2\frac{T_{2,g}T_{2,eff}}{T_g^2}\left(1+T_g^2\Omega^2_{\max}\right)^2}-1\right] \tag{14}$$

A general solution of Eq. (14) with respect to p is obtained in [32]. According to it, the multimode instability may not occur at very low pump rate, when the instability increment Eq. (9) is negative, i.e. for $p<p_{\min}$. The parameter $p_{\min}$ is the pump excess above threshold at which $\Omega^2_{\max}=0$ in Eq. (14) and is given by:

$$\begin{aligned} p_{\min} &= 1+\frac{T_{2,eff}}{T_{2,g}}+\left(\frac{T_1T_{2,eff}}{T_gT_{2,g}}-\frac{T_g^2}{T^2_{2,g}}\right)\left[\sqrt{1+2\frac{T_{2,g}T_{2,eff}}{T_g^2}}-1\right] \\ &\approx 1+\frac{T^2_{2,eff}}{T_g^2}\left[\frac{1}{2}+\frac{T_1}{T_g}\left(1-\frac{T_{2,g}T_{2,eff}}{2T_g^2}\right)\right] \end{aligned} \tag{15}$$

The multimode RNGH self-pulsations may exist only at the pump rates above $p_{\min}$. In long-cavity QCLs, the cavity mode spectrum is dense and the cavity length has no impact on the RNGH self-excitation threshold so as $p_{th2}\approx p_{\min}$. However for the microcavity QCLs (μ-QCLs) with the sparce cavity mode spectrum, the RNGH self-excitation threshold p_{th2} of other cavity modes is higher than $p_{\min}$ because the lowest frequency offset $\Omega_{\max}$ in Eq. (14) at which RNGH instability may occur is $|\Omega^{(th2)}_{\max}|/2\pi=c/Ln_g$ [32], yielding:

$$p_{th2}=1+\theta_{th2}\left(1+\left[\frac{2T_1}{T_g}+\frac{T_{2,g}}{T_{2,eff}}\theta_{th2}\right]^{-1}\right), \qquad \theta_{th2}=\frac{T_1T_{2,eff}}{T_gT_{2,g}}\left[\sqrt{1+2\frac{T_{2,g}T_{2,eff}}{T_g^2}\left(1+\frac{c^2\pi^2T_g^2}{L^2n_g^2}\right)}-1\right] \tag{16}$$

With increasing cavity length L, the instability threshold for self-starting RNGH SPs tends toward $p_{\min}$.

We examine the effect of the magnetic field on QCL lasing dynamics by inspecting the lasing threshold current I_{th} and RNGH instability current $I_{th2}=p_{th2}I_{th}$ behavior as a function of the applied field. More specifically, we have examined the dependence of the actual lasing threshold current change relative to the lasing threshold at zero field in the presence of spatial hole burning, i.e.:

$$\frac{\upsilon(B)\cdot I_{th}(B)}{\upsilon(0)\cdot I_{th}(0)}=\upsilon(B)\cdot Const\cdot\frac{1}{T_1(B)T_{2eff}(B)\mu^2(B)} \tag{17}$$

and the second threshold current change relative to the lasing threshold at zero field in the presence of spatial hole burning:

$$\frac{I_{th2}(B)}{\upsilon(0)\cdot I_{th}(0)}=p_{th2\min}(B)\cdot Const\cdot\frac{1}{T_1(B)T_{2eff}(B)\mu^2(B)} \tag{18}$$

where $Const=T_1(0)T_{2eff}(0)\mu^2(0)/\nu_0(0)$, $\mu=e|d_{3,2}|$ and the dependence of the dipole matrix element for the transition between the upper lasing level 3 and lower lasing 2 on the magnetic field is defined using the perturbation theory approach:

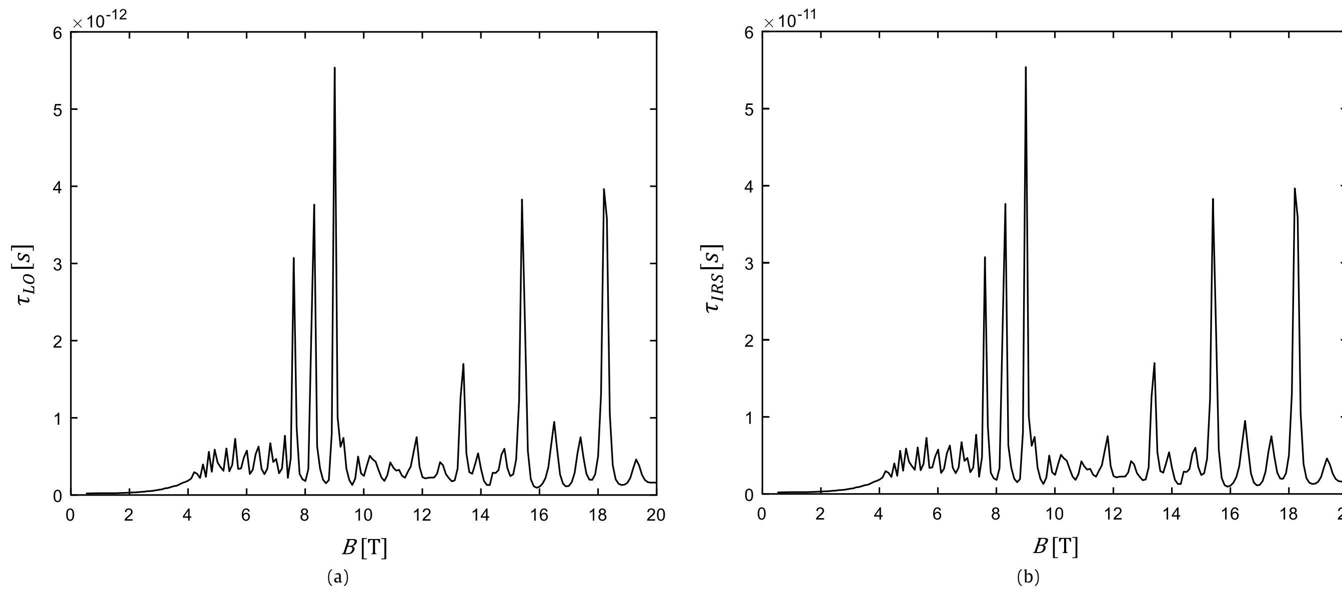

Fig. 1. The dependence of the (a) LO phonon scattering time and (b) the IRS scattering time on the magnetic field value.

$$d_{3,2}(B) = d_{3,2}(0) + \int_{-\infty}^{+\infty} \left(\eta_3^{(1)*} z \eta_{20} + \eta_{30}^{*} z \eta_2^{(1)}\right) dz + \int_{-\infty}^{+\infty} \left(\eta_3^{(1)*} z \eta_2^{(1)}\right) dz \tag{19}$$

Here, the first order correction for envelope wavefunction has the following form (example is given for the upper lasing level): $\eta_3^{(1)} = e\hbar B(j+\frac{1}{2})\sum_{k\neq 3} \frac{M_{3k}}{E_3^{(0)}-E_k^{(0)}}\eta_{k0}$ and $M_{3k} = \int_{-\infty}^{+\infty} \eta_{30}^{*}(\frac{\hat{1}}{M(z)})\eta_{k0} dz$.

In QCLs chips of conventional length (of a few mm long), the gain recovery time is much shorter than the cavity roundtrip time. In the multimode RNGH instability regime they produce multiple irregular self-pulsations within the cavity roundtrip. Only the microcavity QCLs (μ-QCL) with the chip length of hundred microns sustain the regular RNGH self-pulsations. However, their threshold current densities are prohibitively high. In this communication we have shown that by applying a strong magnetic field, it is possible to lower the required pump current for reaching regular RNGH self-pulsations.

3. Numerical results and discussion

Using analytical expressions introduced in the previous chapter, we study the dependence of the RNGH instability threshold, Rabi oscillations frequency, maximum instability increment value and its offset frequency on the magnetic field strength. Although the question in hand is on the broadband multimode emission, lasing spectrum modelling requires numerical simulation with the travelling wave rate equation model (Vukovic JSTQE 2017). These simulations are outside of the scope of the present paper about The calculations were performed for an $In_{0.53}Ga_{0.47}As/Al_{0.48}In_{0.52}As$ QCL structure design with the layer composition and doping profile of the sample N655 from [28]. For evaluating the magnetic field effect on the lasing transition, only the active region of the mentioned structure was analyzed, with the layer thicknesses **43**/17/**9**/54/**11**/53/**12**/47/**22**, where numbers in bold typeface denote the barriers. The electric field bias is fixed at $F = 44$ kV/cm and the lattice temperature is assumed to be $T = 300$ K. The effective masses in the wells and barriers are: $m^*(In_{0.53}Ga_{0.47}As) = 0.042$ and $m^*(Al_{0/48}In_{0.52}As) = 0.075$. The calculated subband energies of the confined states are $E_1 = 0.0575$ eV, $E_2 = 0.0963$ eV, $E_3 = 0.1351$ eV, $E_4 = 0.2983$ eV, $E_5 = 0.3562$ eV, $E_6 = 0.4350$ eV and $E_7 = 0.5004$ eV, with the lasing transition energy being of $\Delta E_{43} = 163$ meV. The structure implements the so-called double LO-phonon resonance design for lower lasing level depopulation, with $\Delta E_{32} = \Delta E_{21} = 38.8$ meV $\approx \hbar\omega_{\mathrm{LO}}$.

The two dominant relaxation mechanisms considered in the model are LO and IRS scattering. The dependence of the LO phonon scattering time, $\tau^{\mathrm{LO}}_{E_i\to E_f} = 1/W\tau^{\mathrm{LO}}_{E_i\to E_f}$, where $W\tau^{\mathrm{LO}}_{E_i\to E_f}$ is given by Eq. (1), and the IRS scattering time, $\tau^{IRS}_{E_i\to E_f} = 1/W\tau^{IRS}_{E_i\to E_f}$, where $W\tau^{IRS}_{E_i\to E_f}$ is given by Eq. (3), on the magnetic field are presented in Fig. 1. The shape of the two curves is imposed by the structure and dispersion of Landau levels and is imprinted on all magnetic field dependences reported below. Note that the LO scattering rate is one order of magnitude higher.

The dependence of the longitudinal relaxation time T_1 is then obtained from the sum of the abovementioned scattering rates, and its dependence on the magnetic field value is shown in Fig. 2a. The transverse relaxation time T_2 obtained from Eq. (6) is plotted as a function of the magnetic field in Fig. 2b. It exhibits much smoother variations in magnetic field as compared to T_1.

Using these data curves, the effective relaxation times, T_g and $T_{2,g}$, as well as the effective transverse relaxation time $T_{2,eff}$ can easily be estimated, which then allow us to find the RNGH instability threshold.

In Fig. 3a, the dependence of p_{th2} in μ-QCL on the magnetic field strength is shown for several microcavity lengths, i.e. 100 µm (blue), 80 µm (red) and 60 µm (green). The minimal (normalized) pump rate $p_{\min}$ to achieve RNGH instability in long-cavity QCLs is plotted in Fig. 3b. The normalized RNGH instability threshold exhibits a general trend to rise with magnetic field. The shorter QCL cavity the higher variations of p_{th2} in the magnetic field, mostly repeating the pattern of T_1 variations from Fig. 2a due to Landau levels.

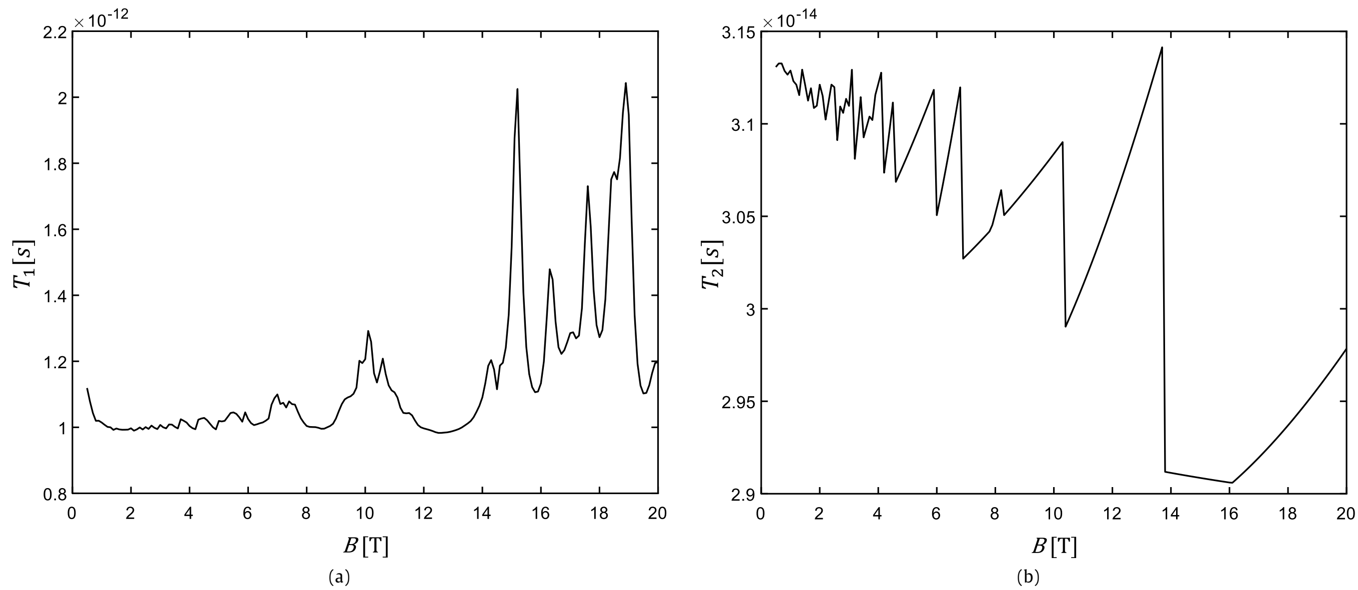

Fig. 2. The dependence of the (a) longitudinal and (b) transverse scattering time on the magnetic field value.

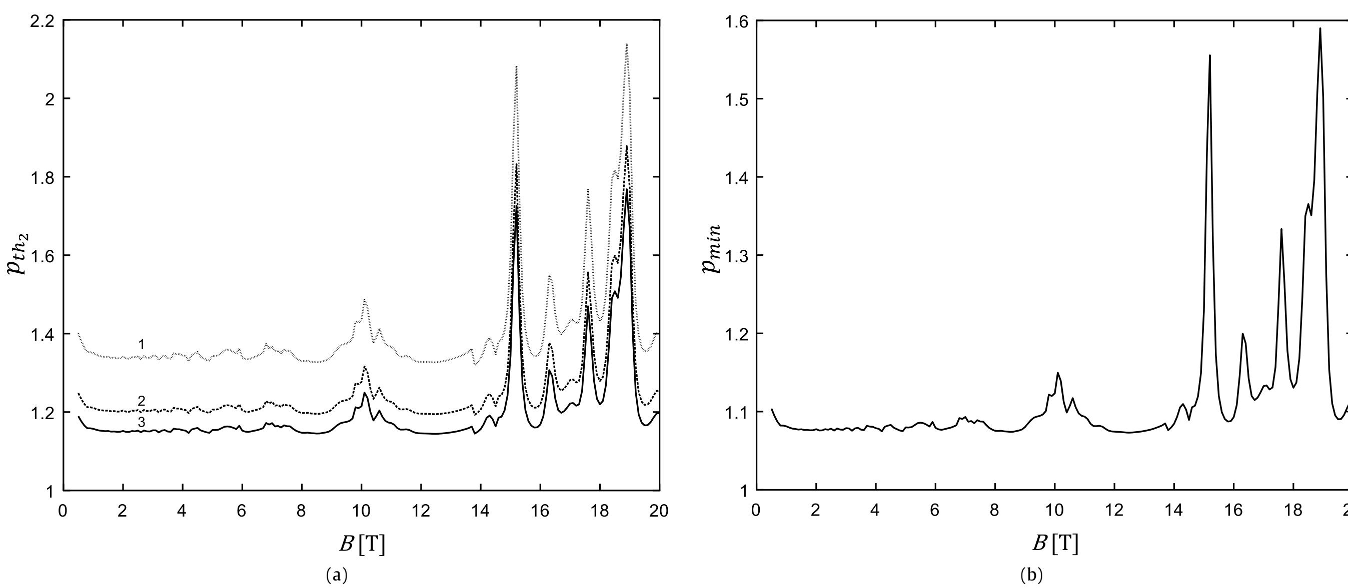

Fig. 3. (a) The dependence of the RNGH instability threshold p_{th2} in μ-QCL on the magnetic field strength for several microcavity lengths, i.e. 100 μm (3), 80 μm (2) and 60 μm (1); (b) Dependence of the minimal pump rate $p_{\min}$ to achieve RNGH instability in long-cavity QCLs plotted as a function of the magnetic field strength.

For the pump excess above the lasing threshold p set to 2.5, the dependence on the magnetic field of the SHB parameter ν_0 from Eq. (13) is represented in Fig. 4. Note that SHB is weakened in strong magnetic fields, which causes the normalized RNGH instability threshold in Fig. 3 to rise.

The Rabi oscillation frequency Ω_{Rabi} and the offset frequency Ω_{max} at the highest RNGH instability increment are shown in Fig. 5. The difference between the two frequencies is caused by the important contribution from the transvers phase relaxation (Fig. 2b). These data curves allow us to find the maximum RNGH instability increment at the offset frequency $\Omega_{\max}$ (see Eq. (11)). In Fig. 6, it is plotted for a fixed pump rate above the lasing threshold of $p = 2.5$, exhibiting a general trend to lower as a function of the magnetic field strength. Like in the case of p_{th2} dispersion, this behavior can be attributed to a reduction of the SHB strength parameter ν_0. Here, the photon lifetime in the cavity is calculated according to the expression $\tau = n_g/cl_0$. The value for l_0, i.e. cavity loss coefficient, comprises of intrinsic material losses and output coupling losses (mirror losses) and is calculated as $l_0 = \alpha_i + \alpha_M$, where $\alpha_M = 1/2\ln(1/(R_1R_2))$.

At first sight, for a fixed pump excess above the lasing threshold p, all these results indicate that the multimode RNGH instability is more difficult to excite in high magnetic fields. However, the lasing threshold current also reduces strongly in the magnetic field, resulting in a completely opposite behavior for a fixed pump current. Thus Fig. 7 shows the actual lasing threshold current change relative to the lasing threshold at zero field in the presence of SHB for a few lowest Landau levels $l = 0$ (1), $l = 1$ (2), $l = 2$ (3) and $l = 3$ (4). The dependence of the 2nd threshold current change relative to the lasing threshold at zero field in the presence of SHB for these Landau levels is given in Fig. 8. It follows that by applying a 10 T (15 T) field, the pumping current required for regular self-pulsations in μ-QCL can be reduced by 50% (80%).

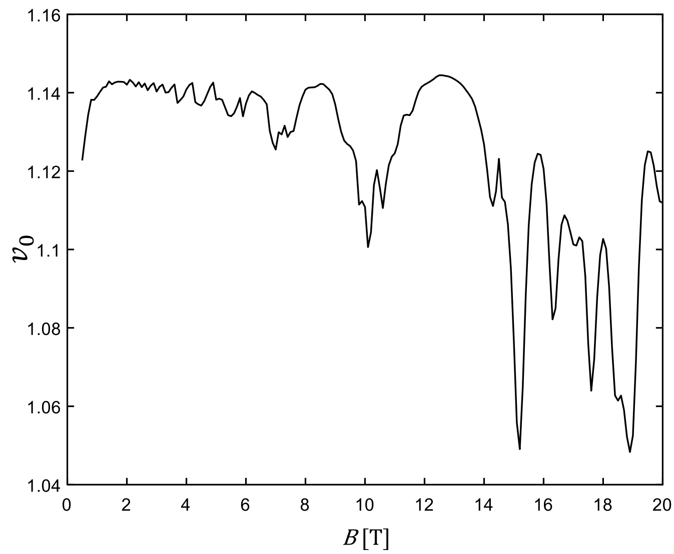

Fig. 4. The dependence of the SHB parameter v_0 on the magnetic field for the pump rate normalized to the lasing threshold in the absence of spatial hole burning of $p = 2.5$.

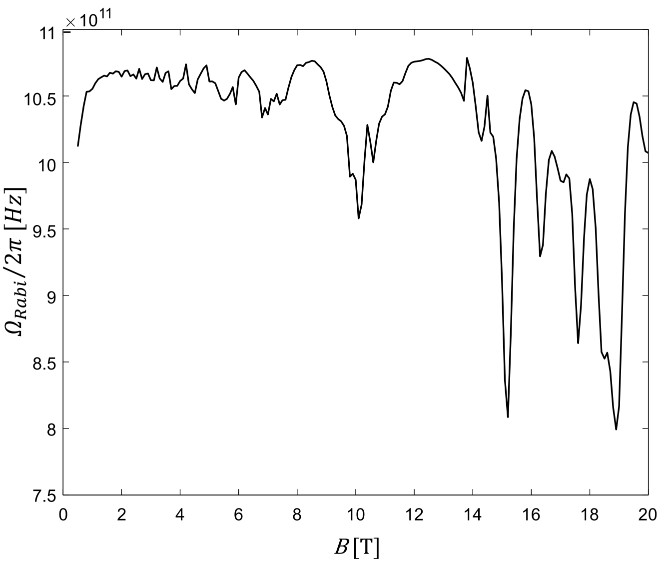

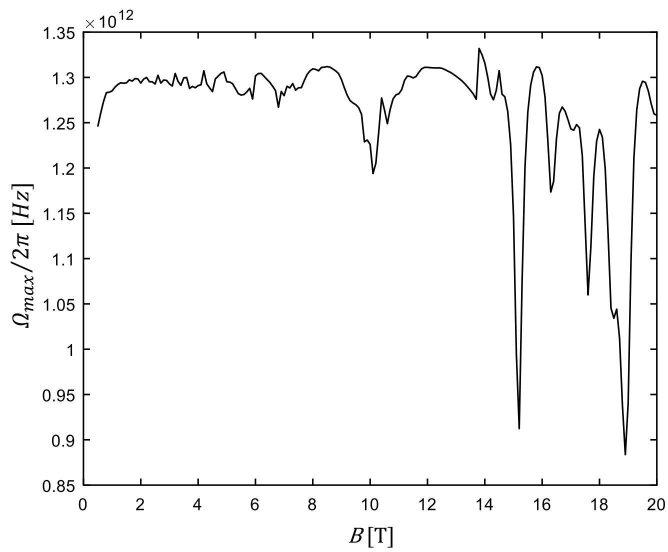

Fig. 5. The (a) Rabi oscillation frequency Ω_{Rabi} and (b) the offset frequency $\Omega_{\max}$ at the highest RNGH instability increment dependence on the magnetic field value. Both frequencies are plotted for the pump rate normalized to the lasing threshold in the absence of spatial hole burning of $p = 2.5$.

4. Conclusion

The magnetic field dependence of the RNGH instability threshold as well as other QCL parameters essential for ultra-fast self-pulsations has been studied on example of microcavity QCLs (μ-QCL). We conclude that the pump current required to reach the broadband multi-mode RNGH self-pulsations is lowered with the magnetic field strength, while the Rabi flopping frequency and the overall optical spectrum width remain practically unchanged. The approach can be helpful for achieving high-power broadband QCL emission in practice, that may be applied to the QCL frequency comb generation. A possibility to further tailor the behavior of QCLs in magnetic field for various specific applications shall be explored in future studies by implementing dedicated QCL designs.

CRediT authorship contribution statement

Aleksandra Gajić: Writing – Original draft preparation, Software, Formal analysis, Methodology. **Jelena Radovanović:** Supervision, Conceptualization, Methodology, Writing - Review & Editing. **Nikola Vuković:** Conceptualization, Methodology, Resources, Software. **Vitomir Milanović:** Supervision, Conceptualization, Methodology, Writing – Review & Editing. **Dmitri L. Boiko:** Writing – Review & Editing, Conceptualization, Methodology.

Declaration of competing interest

The authors declare that they have no known competing financial interests or personal relationships that could have appeared to influence the work reported in this paper.

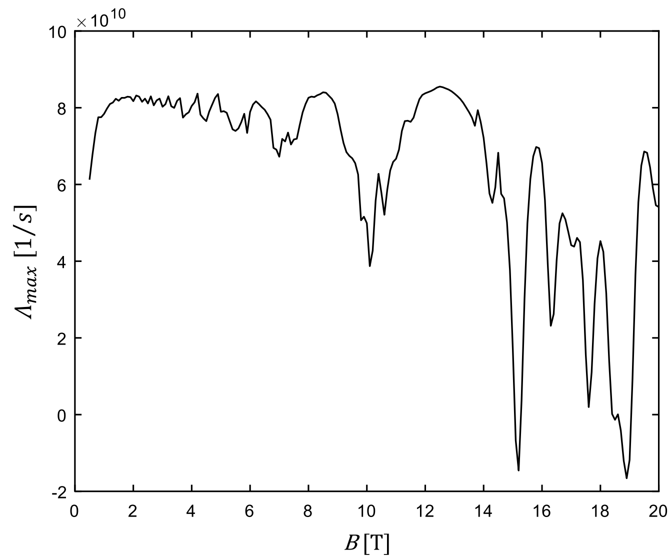

Fig. 6. The dependence of the maximum RNGH instability increment value at the offset frequency $\Omega_{\max}$ on the magnetic field value. The pump rate normalized to the lasing threshold in the absence of spatial hole burning is of $p = 2.5$.

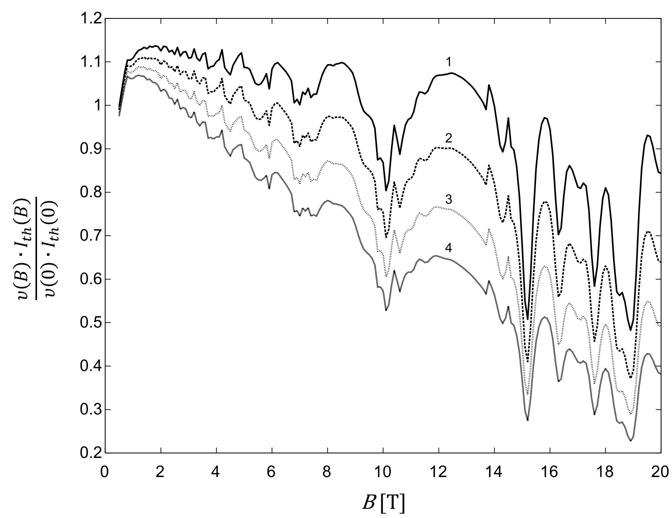

Fig. 7. The actual μ-QCL lasing threshold current change relative to the lasing threshold at zero field in the presence of spatial hole burning depending on the magnetic field and landau index: $l = 0$ (1), $l = 1$ (2), $l = 2$ (3) and $l = 3$ (4).

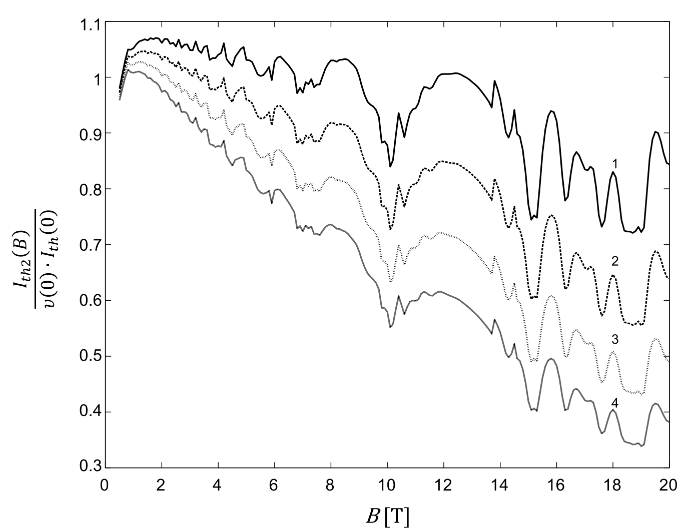

Fig. 8. The dependence of the 2nd threshold current change relative to the lasing threshold in μ-QCL at zero field in the presence of spatial hole burning on the magnetic field value and landau index: $l = 0$ (1), $l = 1$ (2), $l = 2$ (3) and $l = 3$ (4).

Acknowledgements

This work was supported by Swiss National Science Foundation (SNF) project FastIQ, ref. no. IZ73Z0_152761, Ministry of Education, Science and Technological Development (Republic of Serbia), COST ACTIONs BM1205 and MP1204, European Union's Horizon 2020 research and innovation programme (SUPERTWIN, ref. no. 686731) and the Canton of Neuchâtel.

References

[1] J. Alton, S. Barbieri, J. Fowler, H.E. Beere, J. Muscat, E.H. Linfield, D.A. Ritchie, G. Davies, R. Köhler, A. Tredicucci, Magnetic field in-plane quantization and tuning of population inversion in a THz superlattice quantum cascade laser, Phys. Rev. B 68 (2003) 081303, https://doi.org/10.1103/PhysRevB.68.081303.
[2] A.V. Antonov, D.I. Kuritsyn, A. Gajic, E.E. Orlova, J. Radovanovic, V.V. Vaks, D.L. Boiko, Switching on and off the Risken-Nummedal-Graham-Haken instability in quantum cascade lasers, arXiv:1711.10749v1, 2017.
[3] Y.G. Arapov, S.V. Gudina, V.N. Neverov, Temperature dependence of quantum lifetime in n-InGaAs/GaAs structures with strongly coupled double quantum wells, Low Temp. Phys. 39 (2013) 43–49, https://doi.org/10.1063/1.4775751.
[4] S. Barbieri, M. Ravaro, P. Gellie, G. Santarelli, C. Manquest, C. Sirtori, S.P. Khanna, E.H. Linfield, A.G. Davies, Coherent sampling of active mode-locked terahertz quantum cascade lasers and frequency synthesis, Nat. Photonics 5 (2011) 306–313, https://doi.org/10.1038/NPHOTON.2011.49.
[5] C. Becker, C. Sirtori, O. Drachenko, V.V. Rylkov, D. Smirnov, J. Leontin, GaAs quantum box cascade lasers, Appl. Phys. Lett. 81 (2002) 2941–2943, https://doi.org/10.1063/1.1515135.
[6] M. Bugajski, K. Pierściński, D. Pierscinska, A. Szerling, K. Kosiel, Multimode instabilities in mid-infrared quantum cascade lasers, Photonics Lett. Pol. 5 (2013) 85–87, https://doi.org/10.4302/plp.2013.3.02.
[7] D. Burghoff, T-Y. Kao, N. Han, C. Wang, I. Chan, X. Cai, Y. Yang, D.J. Hayton, J-R. Gao, J.L. Reno, Q. Hu, Terahertz laser frequency combs, Nat. Photonics 8 (2014) 462–467, https://doi.org/10.1038/NPHOTON.2014.85.
[8] T. Chakraborty, V. Apalkov, Quantum cascade transitions in nanostructures, Adv. Phys. 52 (2003) 455–521, https://doi.org/10.1080/0001873031000119619.
[9] A.Y. Cho, How molecular beam epitaxy (MBE) began and its projection into the future, J. Cryst. Growth 201–202 (1999) 1–7, https://doi.org/10.1016/S0022-0248(98)01265-2.
[10] A. Daničić, J. Radovanović, V. Milanović, D. Indjin, Z. Ikonić, Magnetic field effects on THz quantum cascade laser: a comparative analysis of three and four quantum well based active region design, Physica E 81 (2016) 275–280, https://doi.org/10.1016/j.physe.2016.03.019.
[11] J. Faist, F. Capasso, D.L. Sivco, C. Sirtori, A.L. Hutchinson, A.Y. Cho, Quantum cascade laser, Science 264 (1994) 553–556, https://doi.org/10.1126/science.264.5158.553.
[12] B. Gelmont, V. Gorfinkel, S. Luryi, Theory of the spectral lineshape and gain in quantum wells with intersubband transitions, Appl. Phys. Lett. 68 (1996) 2171–2173, https://doi.org/10.1063/1.116002.
[13] A. Gordon, C.Y. Wang, L. Diehl, F.X. Kärtner, A. Belyanin, D. Bour, S. Corzine, G. Höfler, H.C. Liu, H. Schneider, T. Maier, M. Troccoli, J. Faist, F. Capasso, Multimode regimes in quantum cascade lasers: from coherent instabilities to spatial hole burning, Phys. Rev. A 77 (2008) 053804, https://doi.org/10.1103/PhysRevA.77.053804.
[14] V. Gorfinkel, S. Luryi, B. Gelmont, Theory of gain spectra for quantum cascade lasers and temperature dependence of their characteristics at low and moderate carrier concentrations, IEEE J. Quantum Electron. 32 (1996) 1995–2003.
[15] R. Graham, H. Haken, Quantum theory of light propagation in a fluctuating laser-active medium, Z. Phys. 213 (1968) 420–450.
[16] A. Hugi, G. Villares, S. Blaser, H.C. Liu, J. Faist, Mid-infrared frequency comb based on a quantum cascade laser, Nature 492 (2012) 229–233, https://doi.org/10.1038/nature11620.
[17] M.V. Kisin, V.B. Gorfinkel, M.A. Stroscio, G. Belenky, S. Luryi, Influence of complex phonon spectra on intersubband optical gain, J. Appl. Phys. 82 (1997) 2031–2038, https://doi.org/10.1063/1.366013.
[18] A. Leuliet, A. Vasanelli, A. Wade, G. Fedorov, D. Smirnov, G. Bastard, C. Sirtori, Electron scattering spectroscopy by a high magnetic field in quantum cascade lasers, Phys. Rev. B 73 (2006) 085311, https://doi.org/10.1103/PhysRevB.73.085311.
[19] H. Li, M. Yan, W. Wan, T. Zhou, K. Zhou, Z. Li, J. Cao, Q. Yu, K. Zhang, M. Li, J. Nan, B. He, H. Zeng, Graphene-coupled Terahertz semiconductor lasers for enhanced passive frequency comb operation, Adv. Sci. 6 (2019) 1900460, https://doi.org/10.1002/advs.201900460.
[20] A. Mottaghizadeh, D. Gacemi, P. Laffaille, H. Li, M. Amanti, C. Sirtori, G. Santarelli, W. Hänsel, R. Holzwart, L.H. Li, E.H. Linfield, S. Barbieri, 5-ps-long terahertz pulses from an active-mode locked quantum cascade laser, Optica 4 (1) (2017) 168–171, https://doi.org/10.1364/OPTICA.4.000168.
[21] M. Razeghi, The MOCVD Challenge: A Survey of GaInAsP-InP and GaInAsP-GaAs for Photonic and Electronic Device Applications, 2nd ed., Taylor & Francis/CRC Press, Boca Raton, FL, USA, 2010.
[22] H. Risken, K. Nummendal, Self-pulsing in lasers, J. Appl. Phys. 39 (1968) 4663, https://doi.org/10.1063/1.1655817.
[23] E. Roldan, G.J. de Valcarcel, F. Prati, F. Mitschke, T. Voigt, Multilongitudinal mode emission in ring cavity class B lasers, in: O.G. Calderon, J.M. Guerra (Eds.), Trends in Spatiotemporal Dynamics in Lasers. Instabilities, Polarization Dynamics, and Spatial Structures, Research Signpost: Trivandrum, India, 2005, pp. 1–80.
[24] M. Rösch, M. Beck, M.J. Süess, D. Bachmann, K. Unterrainer, J. Faist, J. Scalari, Heterogeneous terahertz quantum cascade lasers exceeding 1.9 THz spectral bandwidth and featuring dual comb operation, Nanophotonics 7 (1) (2018) 237–242, https://doi.org/10.1515/nanoph-2017-0024.
[25] D. Smirnov, C. Becker, O. Drachenko, V.V. Rylkov, H. Page, J. Leontin, C. Sirtori, Control of electron-optical-phonon scattering rates in quantum box cascade lasers, Phys. Rev. B 66 (2002) 121305, https://doi.org/10.1103/PhysRevB.66.121305.
[26] D. Smirnov, C. Becker, O. Drachenko, V.V. Rylkov, H. Page, J. Leotin, C. Sirtori, Control of electron–optical-phonon scattering rates in quantum box cascade lasers, Phys. Rev. B 66 (2002) 121305, https://doi.org/10.1103/PhysRevB.66.121305.
[27] D. Smirnov, O. Drachenko, J. Leotin, H. Page, C. Becker, C. Sirtori, V. Apalkov, T. Chakraborty, Intersubband magnetophonon resonances in quantum cascade structures, Phys. Rev. B 66 (2002) 125317, https://doi.org/10.1103/PhysRevB.66.125317.
[28] R. Terazzi, T. Gresch, A. Wittmann, J. Faist, Sequential resonant tunneling in quantum cascade lasers, Phys. Rev. B 78 (2008) 155328, https://doi.org/10.1103/PhysRevB.78.155328.
[29] T. Unuma, M. Yoshita, T. Noda, H. Sakaki, H. Akiyama, Intersubband absorption linewidth in GaAs quantum wells due to scattering by interface roughness, phonons, alloy disorder, and impurities, J. Appl. Phys. 93 (2003) 1586–1594, https://doi.org/10.1063/1.1535733.
[30] N. Vukovic, J. Radovanovic, V. Milanovic, D.L. Boiko, Analytical expression for Risken-Nummedal-Graham-Haken instability threshold in quantum cascade lasers, Opt. Express 24 (2016) 26911–26929, https://doi.org/10.1364/OE.24.026911.
[31] N. Vuković, J. Radovanović, V. Milanović, D.L. Boiko, Multimode RNGH instabilities of Fabrỳ-Pèrot cavity QCLs: impact of diffusion, Opt. Quantum Electron. 48 (2016) 254, https://doi.org/10.1007/s11082--016-0515--s11082-016-0.
[32] N. Vuković, J. Radovanović, V. Milanović, D.L. Boiko, Low-threshold RNGH instabilities in quantum cascade lasers, IEEE J. Sel. Top. Quantum 23 (2017) 1200616, https://doi.org/10.1109/JSTQE.2017.2699139.
[33] C.Y. Wang, L. Diehl, A. Gordon, C. Jirauschek, F.X. Kärtner, A. Belyanin, D. Bour, S. Corzine, G. Höfler, M. Troccoli, J. Faist, F. Capasso, Coherent instabilities in a semiconductor laser with fast gain recovery, Phys. Rev. A 75 (2007) 031802, https://doi.org/10.1103/PhysRevA.75.031802.
[34] C.Y. Wang, L. Kuznetsova, V.M. Gkortsas, L. Diehl, F.X. Kärtner, M.A. Belkin, A. Belyanin, X. Li, D. Ham, H. Schneider, P. Grant, C.Y. Song, S. Haffouz, Z.R. Wasilewski, H.C. Liu, F. Capasso, Mode-locked pulses from mid-infrared quantum cascade lasers, Opt. Express 17 (2009) 12929–12943, https://doi.org/10.1364/OE.17.012929.
[35] G. Zala, B.N. Narozhny, I.L. Aleiner, Interaction corrections at intermediate temperatures: longitudinal conductivity and kinetic equation, Phys. Rev. B 64 (2001) 214204, https://doi.org/10.1103/PhysRevB.64.214204.